
Article:
Liu, D., Gu, D., Smyl, D. orcid.org/0000-0002-6730-5277 et al. (2 more authors) (2019) B-spline level set method for shape reconstruction in electrical impedance tomography. IEEE Transactions on Medical Imaging. ISSN 0278-0062

https://doi.org/10.1109/TMI.2019.2961938

B-spline level set method for shape reconstruction in Electrical Impedance Tomography

Dong Liu, *Member, IEEE*, Danping Gu, Danny Smyl, Jiansong Deng and Jiangfeng Du

***Abstract*— A B-spline level set (BLS) based method is proposed for shape reconstruction in electrical impedance tomography (EIT). We assume that the conductivity distribution to be reconstructed is piecewise constant, transforming the image reconstruction problem into a shape reconstruction problem. The shape/interface of inclusions is implicitly represented by a level set function (LSF), which is modeled as a continuous parametric function expressed using B-spline functions. Starting from modeling the conductivity distribution with the B-spline based LSF, we show that the shape modeling allows us to compute the solution by restricting the minimization problem to the space spanned by the B-splines. As a consequence, the solution to the minimization problem is obtained in terms of the B-spline coefficients. We illustrate the behavior of this method using simulated as well as water tank data. In addition, robustness studies considering varying initial guesses, differing numbers of control points, and modeling errors caused by inhomogeneity are performed. Both simulation and experimental results show that the BLS-based approach offers clear improvements in preserving the sharp features of the inclusions in comparison to the recently published parametric level set method.**

***Index Terms*— Electrical impedance tomography, B-spline level set method, Inverse problems, Shape reconstruction.**

I. Introduction

ELECTRICAL impedance tomography (EIT) is an imaging modality which aims to reconstruct the electrical conductivity of an object by using a set of current injections and voltage measurements usually measured on the object's boundary. Due to the nature of EIT measurements – which are inherently non-invasive, non-intrusive and non-radiative, thereby having no significant side effects – EIT has been used in numerous medical applications, such as respiratory [1] and brain function monitoring [2], and breast cancer detection [3]. Further, EIT has also been utilized for many non-medical industrial applications [4]. For a review of the history, methods and applications of EIT, we refer the reader to [5]–[8].

From a mathematical standpoint, reconstructing a conductivity distribution using EIT is a nonlinear and severely ill-posed inverse problem. Practically speaking, this means that EIT is sensitive to measurement noise and modeling errors [9], [10]. Therefore, regularization techniques are usually essential in solving the inverse problem. The basic idea of regularization is to introduce prior knowledge or constraints to make problem conditionally well-posed. For example, a few of the widely-used regularization methods are smoothness-based techniques implemented using a Tikhonov-type methodology [11], [12], Total Variation (resulting in blocky conductivity distributions) [13], [14], and other sparsity-promoting methods implemented in, for example, compressed sensing [15].

Presently, two major categories of EIT reconstruction methods exist, pixel/voxel-based image reconstruction and shape-based image reconstruction. The pixel/voxel-based image reconstructionb method is an inverse medium problem from noisy observation data – essentially the estimation of a distribution for the unknown conductivity. Some commonly used inverse methods are linearization-based methods [16], [17], the back-projection method [18], direct methods [19]–[22], least-squares methods [10], [12], subspace-based optimization methods [23], statistical inversion methods [24], [25], and learning based methods [26], [27], among other emerging frameworks.

In comparison to the pixel/voxel-based reconstruction methods, the shape-based reconstruction methods focus on detecting the shape of inclusion boundaries as opposed to other information (e.g. absolute conductivity values, other electrical properties, medium composition). Generally, shape-based reconstruction involves a formulation of the inverse problem using a special geometrical representation of the embedded inclusions. Among the methods used for solving the shape reconstruction problem in EIT are ① direct methods, such as the Fourier coefficient based method [28], [29], the factorization method [30], the anomaly detection method [31], the geometric constraint method [32], the monotonicity-based regularization method [33], [34], and the enclosure method [35], [36]; ② indirect methods, such as the moving morphable components based method described in [37].

The level set method, proposed by Osher and Santosa [38], is known to be a versatile tool to automatically tackle the shape and interface evolution. It has been extensively studied for shape reconstruction in EIT [39]–[42], electrical capacitance tomography [43], [44], epitaxial growth [45], electroporation of cell membranes [46] and inverse scattering problems [47]. However, there are numerical concerns associated with this method. For example, in traditional level set (TLS) based methods, re-initialization is usually required to ensure the level set function (LSF) is well behaved and to avoid numerical deterioration of the interface. This process usually adds computational costs to the problem. In addition, the unknown LSF belongs to an infinite dimensional function space. From the perspective of implementation, this requires the discretization of the LSF onto a dense mesh, which tends to be time consuming. In order to overcome these aforementioned problems, parametric level set (PLS) based methods have been proposed in absolute EIT [48], [49] and difference

Manuscript received November 19, 2019; revised December 16, 2019; accepted December 21, 2019. This work was supported in part by the National Natural Science Foundation of China (Grants No. 61871356, No. 81788101, No.11771420 and No. 11761131011), in part by the National Key R&D Program of China (Grant No. 2018YFA0306600), in part by the Chinese Academy of Sciences (Grants No. GJJSTD20170001 and No. QYZDY-SSW-SLH004), and in part by the Anhui Initiative in Quantum Information Technologies (Grant No. AHY050000). (Corresponding author: Dong Liu.)

D. Liu and J. Du are with Hefei National Laboratory for Physical Sciences at the Microscale and Department of Modern Physics, University of Science and Technology of China, Hefei 230026, China, also with CAS Key Laboratory of Microscale Magnetic Resonance, University of Science and Technology of China, Hefei 230026, China, and also with Synergetic Innovation Center of Quantum Information and Quantum Physics, University of Science and Technology of China, Hefei 230026, China (e-mail: dong.liu@outlook.com)

D. Gu and J. Deng are with the School of Mathematical Sciences, University of Science and Technology of China, Hefei 230026, China.

D. Smyl is with the Department of Civil and Structural Engineering, University of Sheffield, Sheffield, UK.

D. Liu and D. Gu contributed equally to this work.

EIT [50]. However, similar to TLS methods, PLS reconstructions often exhibit strong smoothing effects on sharp edges and/or have locally high curvature in the reconstructed shapes, affecting the image quality.

In an effort to preserve sharp properties of reconstructed inclusions, the authors have proposed a direct parameterization method for EIT called the B-spline curve based method [51]. However, this method requires that the number of inclusions in the target domain are known a priori. Pragmatically, one may face problems when such prior information is unavailable. To circumvent this requirement, one possible solution is to integrate a hybrid B-spline and level set regime for automatically tracking the shape evolution. For example, the B-spline based level set (BLS) method has been applied to various applications, e.g., image segmentation [52], tracking left ventricle in cardiac magnetic resonance images [53], micro-mechanical modeling of trabecular bone [54], crack detection [55] and topology optimization [56], [57]. These results demonstrated that the BLS method is suitable for shape reconstruction and offers good approximations of shape boundaries. To the best of our knowledge, the BLS method has yet to be applied to EIT.

Given the recent successes enjoyed by researchers using the BLS method in other fields, we introduce a new BLS method for shape reconstruction in EIT. In the proposed BLS method, the LSF is expressed as a continuous parametric function using B-splines. More precisely, we apply the uniform bi-cubic B-spline surface formula, which is commonly used in geometric design [58], [59] to represent the LSF. In this LSF representation, the BLS method provides several interesting properties enumerated in the following. ① The presentation allows for overall control of the LSF, in contrast to the narrow-band implementation usually applied in TLS [40]. ② The shape reconstruction problem is directly solved in terms of the B-spline coefficients or control points, i.e., once the control points are determined, the shape boundary interface is determined. ③ Re-initialization may be avoided by adding constraints on the B-spline coefficients of the linear expansion. ④ The number of unknowns in the shape reconstruction problem is reduced to the number of B-spline coefficients (control points), which can be significantly smaller than the parametric degrees of freedom used in TLS and traditional pixel-based methods. The dimension reduction therefore reduces the time associated with shape reconstruction and also has significant potential to improve the condition number of the reconstruction problem. ⑤ It provides an evolutionary perspective that not only retains the topological benefits of the implicit representation of evolving boundary (i.e., captures the topology of the inclusions' shape), but also allows for preservation of the inclusions' sharp features. To more succinctly highlight these points, Table I provides a comparison of the geometric representations, sharp property preserving, requirement of priori information, reinitialization, and dimension reduction properties associated with the B-spline curve based direct approach, level set methods and the proposed approach.

In testing the proposed reconstruction regime, we use both simulated and experimental data. The purpose of the numerical and experimental studies are to examine the regime's performance in the context of the most popular EIT biomedical application: lung imaging. In addition, to test the robustness of the BLS method, a set of test cases considering different initial guesses, modeling errors caused by non-homogeneous background, and different numbers of control points are conducted. The results are compared against the PLS reconstructions.

The rest of this paper is structured as follows. In Section II, we briefly review the EIT forward problem. The proposed BLS method is introduced in Section III. Numerical simulations, experimental setup, test cases, implementation details and robustness studies are discussed in Section IV. In Section V, results are presented comparing the performance of the BLS and the PLS methods. Finally, the conclusions are drawn in Section VI.

II. Mathematical description of the forward model

The EIT forward problem refers to the computation of measured voltages from the known injected current and conductivity distributions. Consider a bounded domain $\Omega \in \mathbb{R}^w (w = 2, 3)$ with a boundary $\partial\Omega$. For this geometry, a total number of L electrodes are attached on the boundary from which voltages are measured and currents are injected. For modeling the physics of this problem, we adopt the complete electrode model (CEM) [60], where the electrical potential $u(x, y)$ is the solution of the modified Laplace equation

$$\nabla \cdot (\sigma(x, y)\nabla u(x, y)) = 0, \tag{1}$$

with boundary conditions

$$u(x, y)+z_l\sigma(x, y)\frac{\partial u(x, y)}{\partial n} = U_l, \quad (x, y) \in e_l, l = 1, \ldots, L, \tag{2}$$

$$\int_{e_l} \sigma(x, y)\frac{\partial u(x, y)}{\partial n} dS = I_l, \quad l = 1, \ldots, L, \tag{3}$$

$$\sigma(x, y)\frac{\partial u(x, y)}{\partial n} = 0, \quad (x, y) \in \partial\Omega \backslash \bigcup_{l=1}^{L} e_l. \tag{4}$$

Here, z_l are the contact impedances, n denotes an outward unit normal, and U_l and I_l denote the potential and current with respect to the electrode e_l, respectively.

In addition, in order to ensure the solution's existence and uniqueness, the conservation of charge and potential ground level need to be fixed, i.e.,

$$\sum_{l=1}^{L} I_l = 0, \tag{5}$$

$$\sum_{l=1}^{L} U_l = 0. \tag{6}$$

The numerical solution to the forward model (1-6) is often obtained by using the finite element (FE) approximation [61]. In the FE approximation, the conductivity $\sigma(x, y)$ inside Ω and potential distribution $u(x, y)$ are approximated as

$$\sigma(x, y) = \sum_{k=1}^{N_\sigma} \sigma_k \phi_k(x, y), \tag{7}$$

$$u(x, y) = \sum_{j=1}^{N_u} \alpha_j \psi_j(x, y), \tag{8}$$

where $\phi_k(x, y)$ and $\psi_j(x, y)$ are the nodal basis functions that are used for the conductivity and the potential, respectively. N_σ and N_u are the numbers of nodes in the FE meshes that are used for the representations of $\sigma(x)$ and $u(x)$, α_j are the nodal potentials that are to be determined.

In order to satisfy condition (6), the voltage U is usually represented as a linear combination of $L - 1$ basis functions $n_j \in \mathbb{R}^L$

$$U = \sum_{j=1}^{L-1} \eta_j n_j. \tag{9}$$

Here η_j are the boundary potentials to be determined, and $n_j \in \mathbb{R}^L$ are chosen as $n_1 = (1, -1, 0 \ldots, 0)^{\mathrm{T}} \in \mathbb{R}^L$, $n_2 =$

TABLE I
A COMPARISON OF DIFFERENT SHAPE-BASED RECONSTRUCTION APPROACHES USING B-SPLINE OR LEVEL SET METHOD.

Approaches	Geometry representation	Waiving priori information for number of inclusions	Sharp properties preserving	Dimension reduction	Waiving reinitialization
B-spline curve based approach	Explicit	No	Yes	Yes	Yes
Traditional level set approach	Implicit	Yes	Yes	No	No
Parametric level set approach	Implicit	Yes	No	Yes	Yes
Proposed B-spline-based level set approach	Implicit	Yes	Yes	Yes	Yes

$(1, 0, -1, 0 \ldots, 0)^{\mathrm{T}} \in \mathbb{R}^L$, etc. Then, using a standard Galerkin discretization, the solution

$$(\alpha_1, \ldots, \alpha_{N_{\mathrm{u}}}, \eta_1, \ldots, \eta_{L-1})^{\mathrm{T}} \in \mathbb{R}^{N_{\mathrm{u}}+L-1}$$

to model (1-6) requires solving a system linear equations and finally the measurement U can be computed as $\mathcal{M}\mathcal{D}\eta$, where

$$\mathcal{D} = [n_1, n_2, \ldots, n_{L-1}] \in \mathbb{R}^{L \times L-1}$$

and $\mathcal{M}$ is a difference matrix referred to as the selected measurement pattern.

Next, we denote the discretized forward mapping $\sigma \mapsto U(\sigma)$ by $U(\sigma)$. Assuming the measurement noise is additive and Gaussian the EIT observation model can be expressed as

$$V = U(\sigma) + e, \tag{10}$$

where V is a vector of measured voltages. e is additive Gaussian noise with mean e^* and covariance matrix Γ_e, which are usually experimentally estimated [62]. For more details of the FE approximation used in this paper, we refer the reader to [60], [61].

III. SHAPE RECONSTRUCTION BASED ON B-SPLINE BASED LEVEL SET METHOD

In this section, we introduce the BLS method in which the LSF is expressed as a continuous parametric function using B-splines. For the sake of simplicity, we only consider two-dimensional (2D) cases, and defer three-dimensional cases (3D) in a future work.

A. Shape representation using B-spline based LSF

We begin by defining the LSF $f(x, y)$ as an implicit B-spline function, which is expressed as the linear combination of B-spline basis functions [63].

For the general 2D model, given $(m+1) \times (n+1)$ control points $\{P_{i,j} \in \mathbb{R}^3; i = 0, \ldots, m; j = 0, \ldots, n\}$ in a bi-directional net and noting that $q_{i,j}$ is the z-coordinate of $P_{i,j}$, the tensor-product B-spline function, of degree k in the x-direction and degree l in the y-direction, is a bivariate piecewise polynomial function with the form:

$$f(x, y) = \sum_{i=0}^{m} \sum_{j=0}^{n} N_{i,k}(x) N_{j,l}(y) q_{i,j}, \tag{11}$$

where $N_{i,k}(x)$ and $N_{j,l}(y)$ are the i-th and j-th B-spline basis function of degree k and l, respectively. Further, $q_{i,j}$ forms a net of $(m+1) \times (n+1)$ B-spline coefficients to $f(x, y)$, which can be viewed as control parameters for $f(x, y)$ at the so-called *Greville abscissae* control points. Fig. 1 provides a schematic illustration of a bi-cubic ($k = l = 3$) B-spline based LSF, the corresponding control points, as well as the boundary obtained by assigning $f(x, y) = 0$.

The basis function $N_{i,k}(x)$ is defined by the recurrence relations

$$N_{i,0}(x) = \begin{cases} 1, & x_i \le x < x_i + 1, \\ 0, & \text{otherwise}, \end{cases} \tag{12}$$

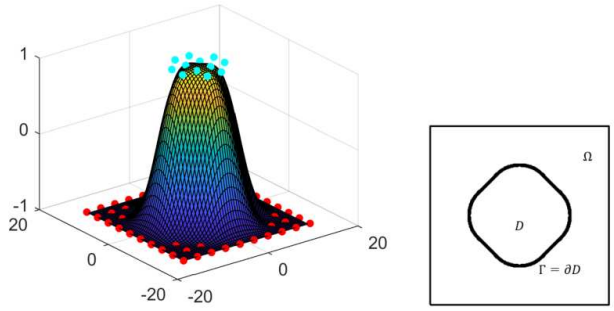

Fig. 1. Illustration of the bi-cubic B-spline based LSF and its control points, as well as the region boundary represented as the zero level set. Left: the red points with z-coordinate $\boldsymbol{q_{i,j} = -1}$ and cyan points with z-coordinate $\boldsymbol{q_{i,j} = 1}$ are control points of the bi-cubic B-spline LSF. Right: the boundary $\boldsymbol{\Gamma}$ obtained from zero level set of bi-cubic B-spline based LSF, i.e., $\boldsymbol{f(x, y) = 0}$.

and

$$N_{i,k}(x) = \frac{x - x_i}{x_{i+k} - x_i} N_{i,k-1}(x) + \frac{x_{i+k+1} - x}{x_{i+k+1} - x_{i+1}} N_{i+1,k-1}(x), \tag{13}$$

where $i = 0, 1, \ldots, m$ and $\{x_i\}_{i=0}^{b}$ is a uniform knot vector with $b = m + k + 1$, defined by

$$x_i = 0, \quad i = 0, 1, \ldots, k, \tag{14}$$

$$x_i = \frac{i - k}{m - k + 1}, \quad i = k + 1, k + 2, \ldots, m, \tag{15}$$

$$x_i = 1, i = m + 1, m + 2, \ldots, m + k + 1. \tag{16}$$

Equations (14) & (16) indicate that the curve in the x direction interpolates at the endpoints. Similarly, $N_{j,l}(y)$ follows the same definition of $N_{i,k}(x)$.

Next, the shape and topology of the inclusions in the object can be described implicitly in the following way

$$\begin{cases} f(x, y) > 0 & \forall (x, y) \in D \backslash \partial D, \\ f(x, y) = 0 & \forall (x, y) \in \partial D, \\ f(x, y) < 0 & \forall (x, y) \in \Omega \backslash D. \end{cases} \tag{17}$$

Here, D denotes a region in Ω bounded by $\Gamma = \partial D$.

B. Modeling the conductivity distribution

Following the common assumption in shape-based reconstruction methods, the conductivity to be estimated is assumed to be piecewise constant. For simplicity, we assume that the domain Ω is divided into two parts: disjoint subregions D and background $\Omega \backslash D$ with piecewise constant conductivity profiles $\sigma(x, y) = \sigma_1$ for $(x, y) \in D$ and $\sigma(x, y) = \sigma_0$ for $(x, y) \in \Omega \backslash D$. In other words, the domain D does not need to be connected and can therefore represent separate inclusions.

In association with the two different regions represented by the B-spline based LSF in (11) & (17), we have the variable (B-spline coefficient) vector

$$\boldsymbol{q} = \{q_{0,0}, \cdots, q_{i,j}, \cdots, q_{m,n}\}, \;\; i = 0, \ldots, m; j = 0, \ldots, n.$$

Moreover, the conductivity distribution $\sigma(x, y)$ in Ω can be written in the form

$$\sigma(x, y, \boldsymbol{q}) = \sigma_0(1 - H_\varepsilon(f(x, y))) + \sigma_1(H_\varepsilon(f(x, y))), \tag{18}$$

where H_ε is a smooth version of the Heaviside function, defined as

$$H_\varepsilon(s) = \begin{cases} 1 & s > \varepsilon, \\ \frac{1}{2}[1 + \frac{s}{\varepsilon} + \frac{1}{\pi}\sin(\frac{\pi s}{\varepsilon})] & |s| \leq \varepsilon, \\ 0 & s < -\varepsilon, \end{cases} \tag{19}$$

and ε is a small positive number that smooths the function.

Now the observation model in (10) can be re-expressed as

$$V = U(\sigma(x, y, \boldsymbol{q})) + e. \tag{20}$$

Following, the problem of shape reconstruction and estimation of piecewise constant conductivities σ_0 and σ_1 is equivalent to solving the following minimization problem

$$[\hat{\boldsymbol{q}}, \hat{\sigma}_0, \hat{\sigma}_1] = \arg\min \Big\{ \|L_e(V - U(\sigma))\|^2 + \lambda_1 \left\|\boldsymbol{q} - \boldsymbol{q}^*\right\|^2 + \lambda_2 \sum_{j=0}^{1} \left\|\sigma_j - \sigma_j^*\right\|^2 \Big\}, \tag{21}$$

where L_e is the Cholesky factor of the inverted noise covariance matrix Γ_e^{-1} (i.e., $L_e^T L_e = \Gamma_e^{-1}$), $\boldsymbol{q}^*$ is a vector of expected values of $\boldsymbol{q}$ and σ_j^* are predetermined constant values. λ_1 and λ_2 are the weighting parameters. The last two terms are regularization functionals, which are used to stabilize the inversion. Note that in the minimization problem (21), unknown σ_0 and σ_1 are appended to the unknown BLS coefficient vector $\boldsymbol{q}$, and are estimated together with $\boldsymbol{q}$ simultaneously.

C. B-spline based level set sensitivity analysis

Due to the nonlinearity and ill-posedness of the minimization problem in (21), the solution is often obtained iteratively. For the optimization regime used herein, the Jacobian matrix $J_U(\boldsymbol{q}, \sigma_0, \sigma_1) = \frac{\partial U}{\partial(\boldsymbol{q}, \sigma_0, \sigma_1)}$ is required. From the chain rule, we can derive the Jacobian of U with respect to the B-spline coefficient vector $\boldsymbol{q}$ as

$$J_U(\boldsymbol{q}) = \frac{\partial U}{\partial \sigma} \cdot \frac{\partial \sigma}{\partial f} \cdot \frac{\partial f}{\partial \boldsymbol{q}} = J_U(\sigma)(\sigma_1 - \sigma_0)\delta(f)\frac{\partial f}{\partial \boldsymbol{q}}. \tag{22}$$

Here, $\delta(f)$ denotes the Dirac function, which is defined as

$$\delta(f) = \frac{\partial H_\varepsilon(f)}{\partial f} = \begin{cases} 0 & |f| > \varepsilon, \\ \frac{1}{2\varepsilon}(1 + cos(\frac{\pi f}{\varepsilon})) & |f| \leq \varepsilon. \end{cases} \tag{23}$$

The term $J_U(\sigma)$ can be computed by using the standard method [12] and $\frac{\partial f}{\partial q}$ can be analytically calculated.

In addition, the Jacobian matrices of the voltage U with respect to the conductivity σ_0 and σ_1 are computed as

$$J_U(\sigma_0) = \frac{\partial U}{\partial \sigma} \cdot \frac{\partial \sigma}{\partial \sigma_0} = J_U(\sigma)(1 - H(f)), \tag{24}$$

and

$$J_U(\sigma_1) = \frac{\partial U}{\partial \sigma} \cdot \frac{\partial \sigma}{\partial \sigma_1} = J_U(\sigma)H(f). \tag{25}$$

Finally, the minimization problem in (21) is solved by using the Gauss-Newton method with a line search algorithm to determine the step size.

TABLE II

DISCRETIZATION DETAILS OF THE COMPUTATIONAL DOMAINS. N_u IS THE NUMBER OF NODES IN THE 2ND ORDER MESH FOR APPROXIMATION OF $u(x, y)$, AND N_σ IS THE NUMBER OF NODES FOR APPROXIMATION OF $\sigma(x, y)$ IN THE 1ST ORDER MESH.

	Simulated data		Reconstruction	
	N_u	N_σ	N_u	N_σ
Cases 1-6&14&15	13301	3382	9656	2436
	Experimental data		Reconstruction	
Cases 7-13			9656	2436

IV. METHODS

In this section, we detail the test cases, finite element discretization, details of implementation, the selection of parameters used in the reconstructions and the studies of robustness. The target conductivity and simulation parameters as well as the experimental configuration are thoroughly detailed in [48], [64]. For the results and discussion, see Section V.

A. Test cases & finite element discretization

To explore the performance of the BLS-based approach, a variety of conductivity distributions exhibiting sharp or smoothed boundaries of two-phase systems were designed. These, in their corresponding test cases, are summarized in the following. The first six test Cases (1-6) consist of studies using simulated data, where we test the regime's ability to reconstruct sharp geometries. Following, in Cases 7-11 and Cases 12 & 13, we study the performance of the BLS approach with low- and high-contrast inclusions using experimental data. The high contrast experimental data in Cases 7-11 was collected with the KIT-4 measurement system [65] developed in University of Eastern Finland and the low contrast experiments (Cases 12 & 13) were carried out with an in-house system (details can be found in [64]) from University of Science and Technology of China. Moreover, the experimental data was taken from a circular tank with a 14cm radius having 16 electrodes of width 2.5cm. The high contrast experiments use saline water with a measured conductivity of 0.543 mS/cm for the background, and resistive (plastic) targets for the inclusions. The low contrast experiments use agar based targets to simulate two lungs and saline with conductivity 1.948 mS/cm for the background.

Further, we conduct a robustness study using geometries from Case 6 considering different initial piecewise constant conductivities. Subsequently, to investigate the regime's robustness to modeling errors generated by inhomogeneity in the background conductivity, additional studies are carried out using inclusion geometries also from Case 6. Finally, we investigate the sensitivity of reconstructions to the number of control points using geometries from Case 4. In all cases, and in order to avoid an 'inverse crime', two different finite element meshes are used for forward and inverse problems. The finite element discretization of the computational domains is given in Table II.

B. Implementation notes

In this subsection, we provide practical information used in implementing the proposed BLS reconstruction approach. For the implementation details related to the PLS method, we refer to our previous works [48], [50].

We begin by setting the degree k and l in (11) as 3, i.e., bi-cubic B-splines are used for expressing the LSF in the BLS method. Next, we address the practicality of selecting control points in BLS. In practice, it is extremely difficult to specify an initial bi-cubic B-spline surface a priori with a suitable number of control points (distributed

appropriately) that would yield a satisfactory shape approximation of the inclusions. For this reason, the number of control points $\mathrm{N_p}$ in both x- and y- directions were set to 10, using trial-and-error. As a result, the total number of control points ($\mathrm{N_p^T}$) totaled $\mathrm{N_p^T} = \mathrm{N_p} \times \mathrm{N_p} = 10 \times 10$. The exception to this is the low contrast experiment studies (Cases 12&13) and robustness study of the BLS method (cf. Section IV-C.3). For these, the dimension of unknown parameter vector (B-spline coefficients) is $\boldsymbol{q} \in \mathbb{R}^{\mathrm{N_p} \times \mathrm{N_p}} = \mathbb{R}^{10 \times 10}$.

During the reconstructions, the initial values to the vector element $q_{i,j}$ in $\boldsymbol{q}$ were randomly assigned. As shown in Fig 2, in the simulated Cases 1-4 and experimental Cases 7-11, z-coordinates, $q_{i,j}$, of 12 control points near the domain center were assigned with positive values, and the other 88 control points were assigned with negative values. The corresponding initial shape interface was determined by the zero level set of $f(x, y)$. Further, the regularization parameters λ_1 and λ_2, in this work were empirically selected as 0.01 and 0.0001, respectively, which are based on trial-and-error method. As an alternative strategy, one could apply the L-curve method to adaptively determine a suitable value to those parameters.

We remark that in the application of lung imaging, we apply prior information related to the approximate location of lung for selecting the initial guesses of $q_{i,j}$. For example, by setting parameters $q_{i,j}$ of the control points located on the left and right sides of the measurement domain to be greater than zero, we initialize two simple shapes as the initial shapes, as shown in Fig. 2 (middle & right).

It is important to remark that in the simulations, we did not use variable vector $\boldsymbol{q}$ to determine the boundary of regions for assigning conductivity profiles. Rather, the regions simulated in the domain were identified with simple mathematical formulas. Therefore, the true variable vector $\boldsymbol{q}$ is unavailable. In the reconstruction, the expected value $\boldsymbol{q}^*$ was set as the randomly selected initial guesses, as noted above. For the shape representation, the smoothed Heaviside function (19) with $\varepsilon = \mathcal{A}/2$ was used. the parameter $\mathcal{A}$, defined as $\mathcal{A} = \frac{\text{Area of domain } \Omega}{\text{Number of elements}}$, denotes the mean value of the element area of the FEM mesh.

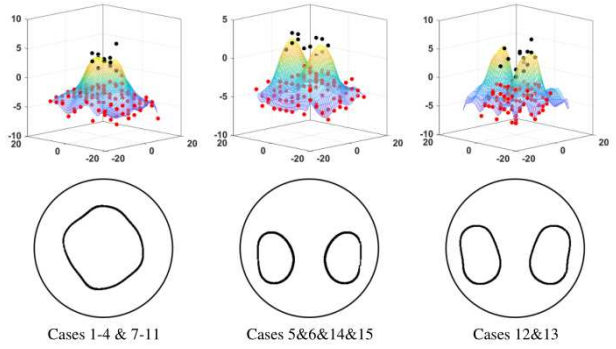

Fig. 2. Illustration of initial setting. Top row: B-spline based LSF and its control points (red points with z-coordinate $\boldsymbol{q_{i,j} < 0}$ and black points with z-coordinate $\boldsymbol{q_{i,j} > 0}$); Bottom row: the region boundary represented as the zero level set, i.e., $\boldsymbol{f(x, y) = 0}$.

Next, in order to set the expected values σ_0^* for the background conductivity and σ_1^* for the inclusion conductivity, we first calculate the best homogeneous estimate $\sigma_{\text{hom}} \in \mathbb{R}$ by solving

$$[\sigma_{\text{hom}}] = \arg\min \left\{ \|L_e(V - U(\sigma))\|^2 \right\}. \tag{26}$$

Then, we set $\sigma_0^* = \sigma_{\text{hom}}$ and $\sigma_1^* = \sigma_{\text{hom}}$ for simulated test cases and low-contrast experimental studies (Cases 12 & 13). In high contrast experimental studies (Cases 7-11), based on the prior information that the plastic objects have almost zero conductivity, we set the expected value $\sigma_1^* = \frac{1}{10}\sigma_{\text{hom}}$ for inclusion conductivity.

To quantitatively assess the recovery of the shape using both the proposed BLS and the reference PLS based methods we calculated the relative size coverage ratio (RCR)

$$\mathrm{RCR} = \frac{\mathrm{CR}}{\mathrm{CR_{True}}}. \tag{27}$$

Here, CR refers to the coverage ratio, which is defined as the ratio of the area of the reconstructed inclusions to the target area; in other words, the measurement domain Ω. $\mathrm{CR_{True}}$ denotes the CR of real inclusion. For example, an RCR value of one means that the area of the reconstructed inclusion is equal to the area of the real inclusion, while a value is less than or greater than one, implies underestimation or overestimation, respectively. The RCR values for the simulations and experiments are shown in Tables III-VI.

For quantifying the estimates of the binary conductivity values of both BLS and PLS based methods, a relative contrast (RCo) was computed, as shown in Tables III-VI, using

$$\mathrm{RCo}_{\sigma_j} = \frac{\widehat{\sigma_j}}{\sigma_j^{\mathrm{True}}}. \tag{28}$$

For practical reasons, we did not compute RCo_{σ_1} in the experimental studies, since the exact conductivity values σ_1 of the inclusions are not accurately known.

In addition, for the simulated test cases, we also use the structural similarity (SSIM) index [66] to evaluate the similarity between true images and reconstructed images. Recall that the maximum SSIM index value of one is achieved if and only if these two images are identical. The SSIM values of simulated cases are shown in Tables III & IV.

C. Robustness studies

To demonstrate the stability of the BLS method, we conducted a set of robustness studies in cases where (i) different initial guesses was assigned to the piecewise constant conductivities, (ii) modeling errors were caused by inhomogeneity in the background and (iii) there were differing numbers of control points.

1) Different initial piecewise constant conductivities: To study the effect of the initial conductivity values on the solution of the BLS method, we performed a set of reconstructions of Case 6 by applying different values to initial conductivity σ_1^* for the inclusions to be detected. For this, we define

$$\sigma_1^* = \eta \sigma_{\text{hom}}, \tag{29}$$

where the parameter η is the initial conductivity coefficient. Here, we set the value of η to change from 0.1 to 1 in a step of 0.1, and a total of 10 images were reconstructed.

2) Non-homogeneous background: In practical medical applications, the conductivity of the background is never purely homogeneous. For example, in lung imaging, inhomogeneities within the human thorax such as heart, aorta, bones, fat, and muscle contrast an otherwise smooth background. For this reason, more realistic conductivities 3.0 mS/cm and 3.1 mS/cm were respectively assigned for the heart and aorta in Cases 14 & 15. Since the conductivity in (18) is modeled as a binary distribution, i.e., the BLS reconstruction approach is restricted to a binary conductivity estimation problem, the presence of the heart and/or aorta in Cases 14 & 15 leads to a situation with non-homogeneous background.

Meanwhile, given the fact that the size/conductivity of lung is much greater/lower than heart and aorta (respectively), the presence of the heart and aorta will be herein considered as modeling error sources in the inversion. Based on these realizations, the robustness study offers an appropriate means to evaluate the performance of BLS with modeling errors due to a non-homogeneous background.

3) Varying number of control points: In general, the B-spline's appearance and complexity are mostly determined by the number of control points, which is chosen using trial-and-error. Theoretically, increasing the number of control points will increase the ability of the B-spline LSF to emulate sharply varying features of the inclusion(s) to be reconstructed. However, it also increases the number of unknowns and adds extra computational cost in the inversion and possibly increases the problem's ill-conditioning.

To investigate the robustness of the BLS approach considering the variability of the number of control points, we carried out a set of reconstructions of Case 4 with the total number of control points $N_p^T = N_p \times N_p = 5 \times 5, 6 \times 6, \cdots, 15 \times 15$, and 20×20.

V. Results

In this section, we first report and compare BLS and PLS reconstructions, using numerical and experimental water tank data. Then, robustness studies of the proposed approach considering non-homogeneous backgrounds, differing initial guesses, and varying number of control points are studied.

A. Reconstruction from simulated data

The results for Cases 1-6 are shown in Fig. 3. The images in the first row depict the ground truth; the BLS and PLS reconstructions are shown in the second and last rows, respectively. For reference, the initial settings of BLS are illustrated in Fig. 2.

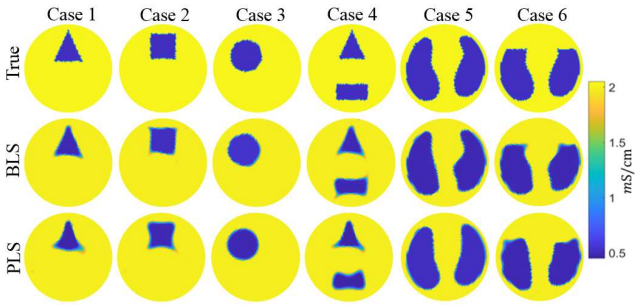

Fig. 3. Reconstructions of Cases 1-6 based on BLS and PLS methods using simulated data.

We observe that both the BLS and PLS methods perform similarly in reconstructing the general inclusion shapes. However, they differ significantly in preserving the sharp boundaries of the inclusions. Indeed, sharp corners (e.g., triangles in Cases 1 & 4 and rectangles in Cases 2 & 4) are (visually) more accurately preserved in BLS reconstructions. This is reflected in Tables III & IV, where the RCRs and RCos corresponding to the BLS method are generally better than those achieved by the PLS method. This is an expected result, since B-spline surfaces are capable of preserving sharp properties – in this situation, this is manifested in the preservation of sharpness at the corners of the inclusions. In contrast, the LSF in the PLS method has a smoothing effect on the sharp corners and high curvature details of shapes in the image, which affects the image quality to some extent.

Based on the former results, it is intuitively interesting to speculate on how the B-spline inclusions evolve during the reconstruction process and how the (possibly) sharp edges of the inclusions form. To illustrate these queries, we show the evolution of the B-spline shapes and topology using odd iteration steps for Case 4 in Fig. 4. From this figure, the evolution of multiple inclusions from a simple initial guess can be clearly observed. Taking a step back, it is intriguing that the entire evolution process in Fig. 4 is largely governed by simply optimizing B-spline coefficients. Moreover, and in comparison to the original B-spline based shape reconstitution approach [51], the proposed BLS method has the advantage that prior knowledge regarding the number of inclusions is not required.

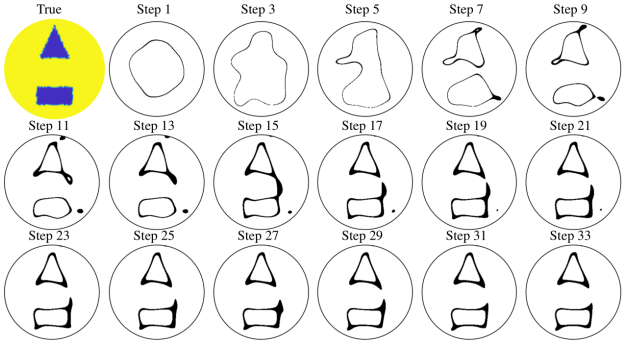

Fig. 4. True image and the evolution of shape and topology, i.e., $\boldsymbol{f}(\boldsymbol{x}, \boldsymbol{y}) = \boldsymbol{0}$, during the BLS reconstruction of Case 4.

B. Reconstruction from phantom data

Figs. 5 & 6 show reconstructions using both BLS and PLS based methods considering *high contrast* and *low contrast* data, respectively. The corresponding evaluation criteria are tabulated in Tables V & VI.

1) High contrast experiments: As the results in Fig. 5 show, the inclusions are clearly distinguishable and the estimated locations correspond to the true shapes in the respective BLS and PLS based reconstructions. Similar to the simulated test cases, both of the BLS and PLS based methods perform well in reconstructing the overall shapes of the inclusions – leading to evaluation criteria approaching the true values, see Table V. Again, BLS reconstructions visually preserve the sharp features of the inclusions, while PLS reconstructions exhibit some distorted inclusions with smoothed properties, e.g., the triangular inclusion in Cases 9 & 11. As a whole, the BLS method generally provides better reconstructions than the PLS method – especially when the target is geometrically complex.

It is worth remarking that, compared to that reconstruction using the PLS method, the circular inclusions in Cases 9-11 were unfavorably tracked by BLS method, which is an expected result. The main reason is that, principally, uniform bi-cubic B-spline surface formula is unable to exactly represent a circle shape [67]. In contrast, the PLS function is able to capture such a shape.

Note that, for the sake of comparison to other shape-based estimates, e.g., traditional level set (TLS) method, we recall our previous results for the same test cases using TLS method in Fig. 4 from [48]. We observe that the BLS-based estimate is clearly better than the TLS-based estimate, even when a coarser mesh is used for the BLS-based estimate wherein more discretization error may arise in the reconstruction.

2) Low contrast experiments: Fig. 6 shows the results of both methods considering two experimental low contrast test Cases (12 & 13). Once again, the lung-type inclusions are successfully detected by both methods, although the contrast of the inclusions made of agar with respect to the background filled with saline is much lower than that in Cases 7-11 (plastic objects vs. saline). Based on visual assessment, the BLS method provides slightly better reconstructions of the lobe part of the lung-type inclusions, where the sharp properties are smoothed away by the PLS based reconstructions. This finding is consistent with the results obtained in simulated and experimental high contrast cases.

Owing to the fact that the lung-type shapes are relatively complex, the dimension of the control points net was increased to $N_p^T = 15 \times 15$ in these reconstructions to improve the ability of the B-spline LSF to emulate sharply varying features of the lung-type inclusions.

TABLE III

EVALUATION CRITERION: RCRS,SSIM INDICES AND RCO OF CASES 1-4.

	Case 1				Case 2				Case 3				Case 4				
	SSIM	RCR	RCoσ_0	RCoσ_1	SSIM	RCR	RCoσ_0	RCoσ_1	SSIM	RCR	RCoσ_0	RCoσ_1	SSIM	$\mathrm{RCR_T}$	$\mathrm{RCR_B}$	RCoσ_0	RCoσ_1
True	1.00	1.00	1.00	1.00	1.00	1.00	1.00	1.00	1.00	1.00	1.00	1.00	1.00	1.00	1.00	1.00	1.00
BLS	0.98	0.97	1.00	0.99	0.98	0.96	1.00	1.01	0.98	1.01	1.00	1.09	0.97	0.95	0.95	1.00	0.98
PLS	0.98	0.92	1.00	0.93	0.98	0.91	1.00	0.95	0.97	0.95	1.00	0.97	0.96	0.94	0.94	1.00	0.94

The subscript letters 'T' and 'B' under the parameter RCR denote the top and bottom objects in the domain, respectively.

TABLE IV

EVALUATION CRITERION: RCRS,SSIM INDICES AND RCO OF SIMULATED LUNG IMAGING TEST CASES 5,6,14&15.

	Case 5					Case 6					Case 14					Case 15				
	SSIM	$\mathrm{RCR_L}$	$\mathrm{RCR_R}$	RCoσ_0	RCoσ_1	SSIM	$\mathrm{RCR_L}$	$\mathrm{RCR_R}$	RCoσ_0	RCoσ_1	SSIM	$\mathrm{RCR_L}$	$\mathrm{RCR_R}$	RCoσ_0	RCoσ_1	SSIM	$\mathrm{RCR_L}$	$\mathrm{RCR_R}$	RCoσ_0	RCoσ_1
True	1.00	1.00	1.00	1.00	1.00	1.00	1.00	1.00	1.00	1.00	1.00	1.00	1.00	1.00	1.00	1.00	1.00	1.00	1.00	1.00
BLS	0.95	0.95	1.00	1.00	1.00	0.96	0.96	0.99	1.00	1.00	0.98	0.91	0.96	1.00	0.97	0.97	0.90	0.95	1.00	0.97
PLS	0.95	0.99	0.96	1.00	1.00	0.92	0.96	1.03	1.00	0.99	0.95	0.94	0.92	1.00	0.97	0.95	0.92	0.91	1.00	0.96

The subscript letters 'L' and 'R' under the parameter RCR denote the left and right side objects in the domain, respectively.
To avoid the influence arising from the inhomogeneity, the true image of Case 5 was used as the reference image for computing the SSIM in Cases 14&15.

As a result of the refined control-point net, BLS reconstructions in Fig. 6 contain some edge artifacts or serration. Moreover, by refining the control points, the dimension of unknown vector $\boldsymbol{q}$ increases to $\mathbb{R}^{225}$. This results in an increasingly ill-posed problem compared to situations using fewer control points. The effect of the control point net refinement is further investigated in Section V-C.3.

It is worth remarking that, in this paper, the selection of control point net was done by trial-and-error procedure and is therefore not optimal. Better selection may be conducted by interpreting the optimal number of control points as a model selection problem [68], [69]. However, the main purpose of this paper is to focus on shape reconstruction using BLS, thus optimizing the number of control points of the B-spline surface is excluded herein.

C. Results of robustness studies

1) Effect of initial piecewise constant conductivity: Fig.7 shows two representative reconstructions from a sequence of ten images obtained with the BLS approach. The corresponding SSIM, RCR and RCo of these ten images are shown in Fig. 9 (left). We observe that the lung shapes are relatively well estimated and the evaluation criteria show that the BLS method is quite robust to different initial piecewise constant conductivity values.

2) Effect of non-homogeneous background: Fig. 8 shows the BLS and PLS based reconstructions for Cases 14 & 15, where the inhomogeneities are presented in the measurement domain. We observe that the performance of both methods compared to each other remains similar to the more ideal case (Case 5); Compared to PLS, BLS gives a slightly better estimate to the inner lung shape, especially for the right upper lobe. This observation is supported by the metrics parameters SSIM and $\mathrm{RCR_R}$ listed in Table IV.

There are two additional, yet subtle, realizations that can be made from Fig. 8, namely (i) it seems that the presence of heart and aorta does not largely affect the reconstructions and (ii) in BLS reconstructions, there are few edge artifacts presented along the right outer boundary. Regarding comment (i), the primary explanation is that EIT measurements are much more sensitive to large inclusions with low conductivity and less sensitive to small inclusions with high conductivity. As such, even though the heart and aorta have relative high conductivity values, the shape reconstruction also tends have higher sensitivity to the main component of the measurement – the lungs. This finding and features are in agreement with the results from previous works using PLS [48], B-spline [51] and moving morphable components based reconstructions [37]. Regarding comment (ii), some possible explanations include: non-optimized selection of control points, modeling errors due to the non-homogeneous background and the ill-posedness of the EIT reconstruction problem.

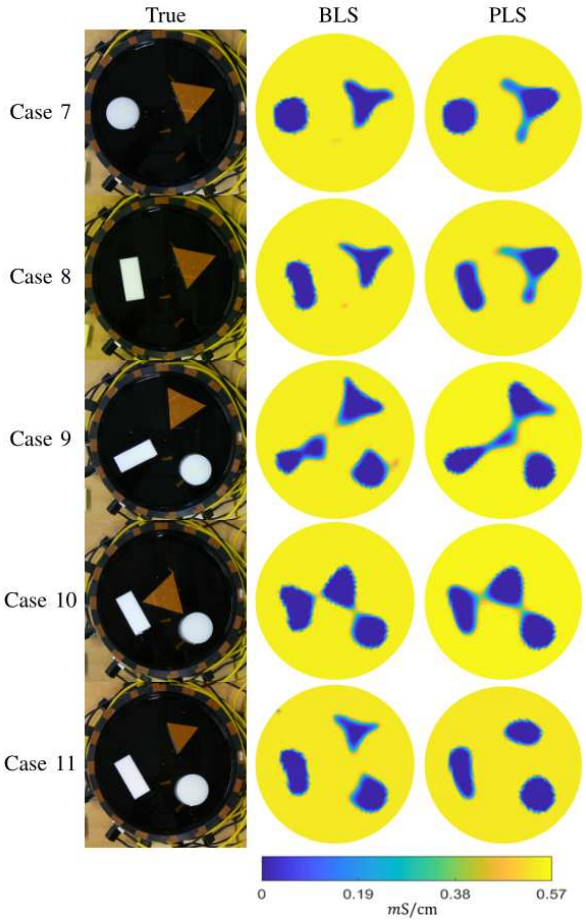

Fig. 5. Reconstructions of Cases 7-11 based on BLS and PLS methods using *high contrast* phantom data, in which the inclusions were made of plastic material.

3) Effect of the number of control points: BLS-based reconstructions for Case 4 with differing numbers of control points $\mathrm{N_p^T}$ are shown in Fig. 10. Images shown in Fig. 10 clearly illustrate the effects of using differing numbers of control points on BLS reconstructions. An expected result here is that the sharpness of the reconstructions is generally better preserved in reconstructions using more control points. Although, there is certainly a correlation between using a large number of control points to improve sharpness and the presence of edge artifacts; these points are discussed in the following.

Based on the visual observations, we preliminarily conclude that the preservation of sharpness in reconstructions using a larger number of control points results from one primary factor – increasing $\mathrm{N_p^T}$ will

TABLE V

THE RELATIVE SIZE COVERAGE RATIOS (RCRS) AND RCO OF THE RECONSTRUCTED $\boldsymbol{\sigma_0}$ IN STUDIES WITH PHANTOM DATA.

	Case 7			Case 8			Case 9			Case 10				Case 11			
	RCR_c	RCR_t	$RCo\sigma_0$	RCR_r	RCR_t	$RCo\sigma_0$	RCR_t	RCR_r	RCR_c	$RCo\sigma_0$	RCR_t	RCR_r	RCR_c	$RCo\sigma_0$	RCR_t	RCR_r	RCR_c	$RCo\sigma_0$
True	1.00	1.00	1.00	1.00	1.00	1.00	1.00	1.00	1.00	1.00	1.00	1.00	1.00	1.00	1.00	1.00	1.00	1.00
BLS	0.97	0.97	1.01	1.04	0.93	1.01	1.02	0.96	0.92	1.02	0.98	1.09	0.96	1.02	0.93	0.95	0.93	1.00
PLS	1.00	1.04	1.01	0.98	1.08	1.01	0.98	1.07	0.91	1.02	1.03	1.03	1.01	1.02	0.96	1.01	0.95	1.00

The subscript letters 'c', 't' and 'r' under the parameter RCR denote circle, triangle and rectangle, respectively.

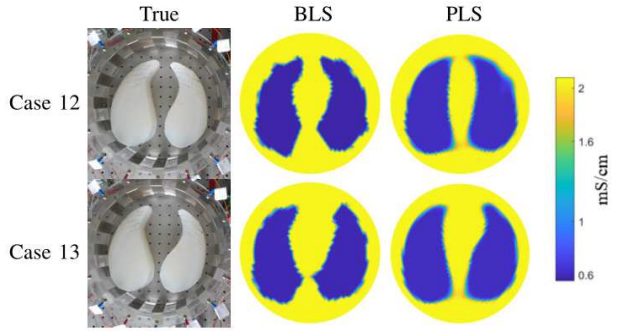

Fig. 6. Reconstructions of Cases 12 & 13 based on BLS and PLS methods using *low contrast* phantom data, in which lung-type inclusions were made of agar.

TABLE VI

THE RELATIVE SIZE COVERAGE RATIOS (RCRS) AND RCO OF THE RECONSTRUCTED $\boldsymbol{\sigma_0}$ IN LUNG PHANTOM STUDIES.

	Case 12			Case 13		
	RCR_L	RCR_R	$RCo\sigma_0$	RCR_L	RCR_R	$RCo\sigma_0$
True	1.00	1.00	1.00	1.00	1.00	1.00
BLS	0.98	1.03	1.05	1.02	1.01	1.04
PLS	1.02	1.03	1.05	1.02	1.02	1.05

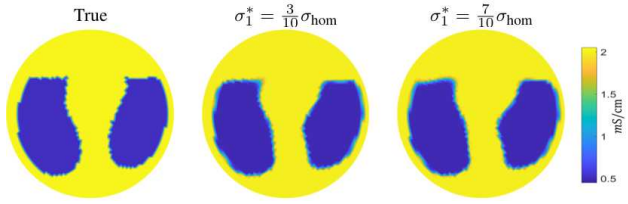

Fig. 7. BLS reconstructions for Case 6 with different initial piecewise conductivity values.

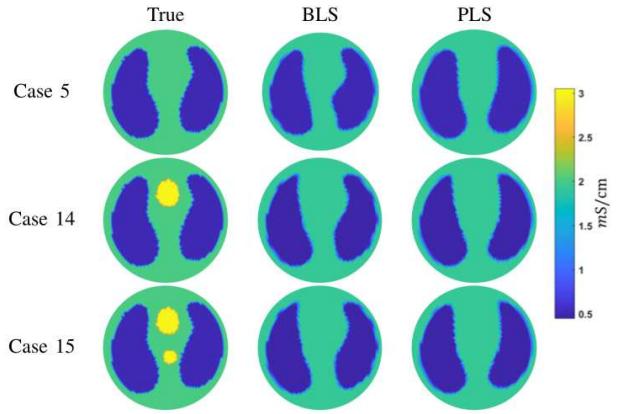

Fig. 8. BLS and PLS based reconstructions for lung imaging with and without non-homogeneous background. The first row is a repetition of the fifth row in Fig.3.

increase the ability of the B-spline LSF to emulate sharply varying features of the inclusions. This is also compatible with a fundamental concept of B-spline surfaces – the use of more control points results in more local control and capacity to express topological discontinuities and complicated shapes. However, similar to the reconstructions of low-contrast experimental cases shown in Fig. 6, some edge artifacts or serration are observed in the images corresponding to the relatively large number of N_p^T (increasing the ill-conditioning/ill-posedness of the problem). On the other hand, using too few control points (i.e. $N_p^T = 5 \times 5$) results in blurred image since the BLS method cannot adequately depict a complex geometry.

To more comprehensively and quantitatively show the effect of the number of control points in BLS method, we compute the evaluation criteria (RCR/RCo/SSIM), which are plotted in Fig. 9 (middle). The criteria shown in Fig. 9 (middle) indicate expected trends, (a) the selection of differing N_p^T results in relative in-variance of the RCos using the BLS method, (b) the SSIM approaches the true value (1.0) with increasing number of control points, and (c) the RCRs predominately increase proportional to N_p^T. Consistent with visual observations from the reconstructed images shown earlier, the BLS reconstruction approach is quite robust to the selection of different number of control points.

D. Discussion: limitations, multiphase and further developments

The proposed BLS-based shape reconstruction method is presently limited by its nonlinearity and non-optimized selections of the parameters. As such, a number of issues need to be considered in the future works. These key issues are enumerated in the following.

1) Due to the reality that BLS method is rooted in the context of absolute imaging, the reconstruction problem is solved iteratively. This requires repetitive calculation of the forward problem, mostly in the line-search. Consequently, this process can be fairly time consuming, which is one of the present drawbacks. As an example, reconstructions of Case 5 were obtained from a Matlab implementation of the proposed BLS and reference PLS methods on a desktop computer with an Intel Xeon E3-1231 processor and 16GB memory within 20 iterations at average speed of 45 seconds per iteration, and 18 iterations at average speed of 41 seconds per iteration, respectively. As a whole, the computational cost in each iteration of BLS is comparable to PLS.
   It is also important to study the convergence behavior of both methods, as shown in Fig. 9 where we plot the root mean square error (RMSE) of the estimated conductivity against the iteration steps for both methods in Case 5. Overall, the computing time required for each test case varies depending on a number of factors, including the number of control points and the level of FEM discretization, etc. To speed up the reconstruction, one possible option is to formulate the nonlinear shape reconstruction approach using a linearization approximation, since the inclusion information (e.g., support of shape) in EIT is in some sense invariant under linearization [70]. However, this reduction in computing cost is likely at the expense of reducing image resolution.
2) It is well known that absolute imaging is sensitive to modeling errors arising from electrode displacement and inaccurate

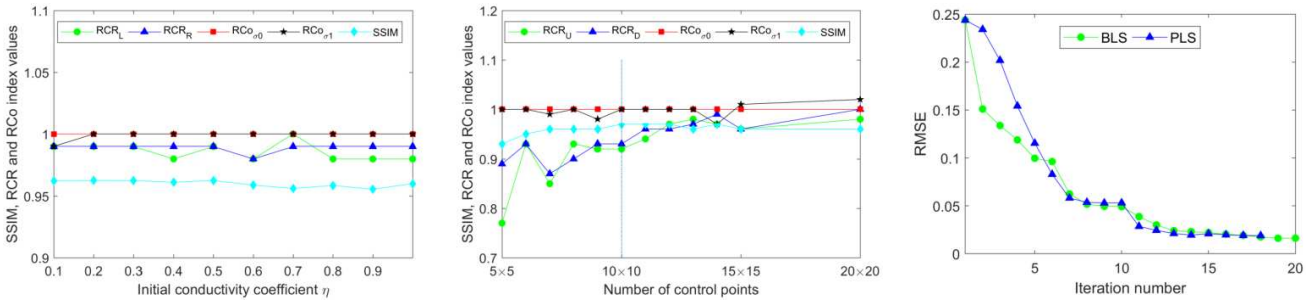

Fig. 9. Performance evaluation of BLS based reconstruction. Left: evaluation criteria of the robustness study against different initial conductivity value reported in subsection IV-C.1. Middle: evaluation criteria of the robustness study against different control points reported in subsection IV-C.3. Right: root mean square error through the iterative process of Case 5 shown in Fig.3.

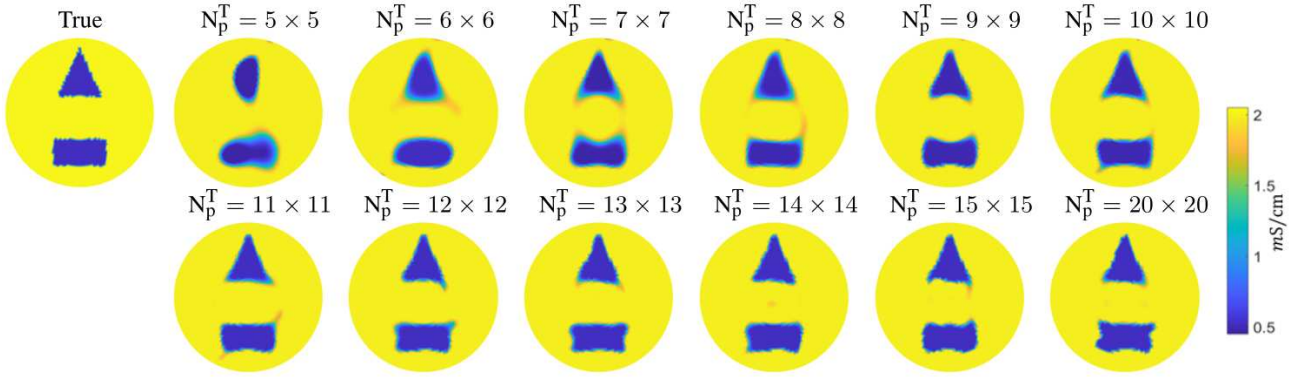

Fig. 10. Robustness study of the proposed BLS method *w.r.t* different number of control points N_p^T.

knowledge of the measurement domain boundary, etc. Hence, much additional work needs to be done to explore the BLS method's robustness to modeling errors. Possible solutions for improving the method's tolerance to modeling errors are ① to apply the approximation error approach to compensate for these modeling errors [24], ② to frame the shape reconstruction approach in a linear difference imaging context, which is known to be quite robust to these sources of modeling errors, and ③ to consider the shape reconstruction problem in the framework of multi-frequency EIT [71]. Clearly, this matter is beyond the scope of this paper and is planned to be studied in a future work.

3) The selection of control points net was done by trial-and-error procedure and is therefore not optimal. Except the potential solution mentioned in Section V-C.3, one may also consider through the addition of adding new control points to gain more refined shape control or the removal of redundant control points to generate a B-spline surface with as few control points as possible that approximates a given shape.
4) The current work focused on the shape reconstruction with binary conductivities, an interesting question arising in the multiphase system (e.g., thorax imaging) is: *Is the proposed BLS-based approach able to reconstruct the heart and/or aorta together with lung?* To deal with this question, one potential solution is to apply multiple LSFs to model the boundary shapes of lungs and heart/aorta. A similar strategy used for PLS-based multiphase conductivity estimation problem was suggested in [49]. In addition, all the subregions of the test cases presented in the measurement domain are assumed to be simply disconnected. However, in real applications of lung monitoring, some cancers that may appear as a mass in the lungs include lymphomas and sarcomas. While this is certainly true, the proposed method is not presently designed for this type of lung monitoring. Nonetheless, one may extend the proposed method by treating the reconstruction problem as a nested case and use multiple B-spline-based LSFs for modeling conductivity distribution for nested inclusions, as illustrated in Fig. 11. However, studying the implementation of B-spline-based multiphase reconstruction framework is out of the scope of this paper, hence it is left for future research.
5) Until this point, only low-conductivity inclusions are used throughout the paper. Another interesting question arising here is: *does the method still work well in the case of a binary conductivity distribution wherein the conductivity of the inclusions is greater than that of the background?* To gain insight into this question, we computed the simulated test cases shown in Fig. 12. Obviously, the proposed BLS method still works well, producing good shape reconstructions, which is also confirmed by the criteria SSIM=0.96, $\mathrm{RCR}_{\mathrm{top}} = 0.87$, $\mathrm{RCR}_{\mathrm{bottom}} = 0.98$, $\mathrm{RCR}_{\sigma_0} = 0.99$ and $\mathrm{RCR}_{\sigma_1} = 1.02$.
6) Lastly, the proposed BLS method is only tested with 2D examples. However, its capacity for 3D reconstructions is more pronounced when the difference between the number of voxels

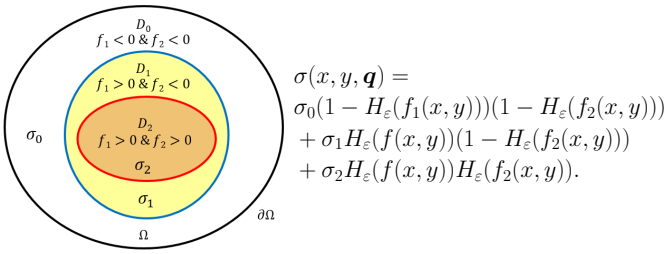

Fig. 11. Modeling conductivity distribution of nested cases using multiple LSFs.

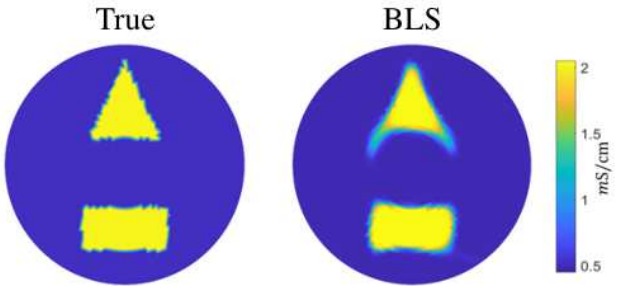

Fig. 12. BLS reconstructions for Case 16 with conductivity of the inclusions is greater than that of the background.

and the number of B-spline coefficients is more significant. Heuristically, to represent and to reconstruct the 3D geometry, one may consider formulating the LSF as a trivariate B-spline function and then follow the same strategies used in the proposed method to formulate the minimization problem in (21). For 3D modeling using B-spline based LSF, we refer the readers to the recent work in the field of shape and topology optimization [57]. In addition, the current work is focused on EIT. One may also consider to extend the proposed method to other imaging modalities, e.g., microwave imaging [72]. It should be mentioned that, the study of 3D situations through the proposed methodology framework and the extension to other imaging modalities are an important future direction.

VI. Conclusions

In this paper, we considered shape reconstruction in electrical impedance tomography. In the proposed BLS method, the inclusions' shapes to be reconstructed are implicitly represented by a level set function, which is modeled as a continuous parametric function expressed using B-spline functions.

We tested the performance of the proposed method with both simulated examples as well as real tank measurement cases, both corresponding to lung imaging (absolute) shape reconstruction problems. The results illuminate the ability of the BLS method to preserve sharp features of the inclusions, as well as to automatically track the (unknown) number of inclusions present in the domain. Meanwhile, it was demonstrated that the BLS method is quite robust to the initial piecewise constant conductivity distribution and differing numbers of control points. The BLS method is also tolerant to the modeling errors caused by the presence of inhomogeneities in the background to some extent. The findings demonstrate that BLS has important potential to be a generalized technique for integrating the priori shape information into EIT image reconstruction.

References

[1] P. A. Muller, J. L. Mueller, M. Mellenthin, R. Murthy, M. Capps, B. D. Wagner, M. Alsaker, R. Deterding, S. D. Sagel, and J. Hoppe, "Evaluation of surrogate measures of pulmonary function derived from electrical impedance tomography data in children with cystic fibrosis," *Physiological measurement*, vol. 39, no. 4, p. 045008, 2018.

[2] K. Y. Aristovich, B. C. Packham, H. Koo, G. S. dos Santos, A. McEvoy, and D. S. Holder, "Imaging fast electrical activity in the brain with electrical impedance tomography," *NeuroImage*, vol. 124, pp. 204–213, 2016.

[3] E. K. Murphy, A. Mahara, and R. J. Halter, "Absolute reconstructions using rotational electrical impedance tomography for breast cancer imaging," *IEEE Transactions on Medical Imaging*, vol. 36, 4 2017.

[4] J. Yao and M. Takei, "Application of process tomography to multiphase flow measurement in industrial and biomedical fields - a review," *IEEE Sensors Journal*, vol. 17, no. 24, pp. 8196–8205, 2017.

[5] D. Holder, *Electrical impedance tomography: methods, history and applications*. CRC Press, 2004.

[6] R. Harikumar, R. Prabu, and S. Raghavan, "Electrical impedance tomography (eit) and its medical applications: a review," *Int. J. Soft Comput. Eng*, vol. 3, no. 4, pp. 193–198, 2013.

[7] T. K. Bera, "Applications of electrical impedance tomography (eit): a short review," in *IOP Conference Series: Materials Science and Engineering*, vol. 331, no. 1. IOP Publishing, 2018, p. 012004.

[8] T. A. Khan and S. H. Ling, "Review on electrical impedance tomography: Artificial intelligence methods and its applications," *Algorithms*, vol. 12, no. 5, p. 88, 2019.

[9] E. K. Murphy and J. L. Mueller, "Effect of domain shape modeling and measurement errors on the 2-d d-bar method for eit," *IEEE transactions on medical imaging*, vol. 28, no. 10, pp. 1576–1584, 2009.

[10] D. Liu, V. Kolehmainen, S. Siltanen, A.-M. Laukkanen, and A. Seppänen, "Nonlinear difference imaging approach to three-dimensional electrical impedance tomography in the presence of geometric modeling errors," *IEEE Transactions on Biomedical Engineering*, vol. 63, no. 9, pp. 1956–1965, 2016.

[11] B. Jin and J. Zou, "Augmented tikhonov regularization," *Inverse Problems*, vol. 25, no. 2, p. 025001, 2009.

[12] M. Vauhkonen, D. Vadasz, P. A. Karjalainen, E. Somersalo, and J. P. Kaipio, "Tikhonov regularization and prior information in electrical impedance tomography," *IEEE transactions on medical imaging*, vol. 17, no. 2, pp. 285–293, 1998.

[13] J. Yoon Mo and Y. Sangwoon, "Impedance imaging with first-order tv regularization," *IEEE Transactions on Medical Imaging*, vol. 34, no. 1, pp. 193–202, 2015.

[14] G. González, J. M. J. Huttunen, V. Kolehmainen, A. Seppänen, and M. Vauhkonen, "Experimental evaluation of 3d electrical impedance tomography with total variation prior," *Inverse Problems in Science and Engineering*, no. 8, pp. 1–21, 2015.

[15] S. Liu, J. Jia, Y. D. Zhang, and Y. Yang, "Image reconstruction in electrical impedance tomography based on structure-aware sparse bayesian learning," *IEEE transactions on medical imaging*, vol. 37, no. 9, pp. 2090–2102, 2018.

[16] M. Cheney, D. Isaacson, J. C. Newell, S. Simske, and J. Goble, "Noser: An algorithm for solving the inverse conductivity problem," *International Journal of Imaging Systems and Technology*, vol. 2, no. 2, pp. 66–75, 1990.

[17] A. Adler, J. H. Arnold, R. Bayford, A. Borsic, B. Brown, P. Dixon, T. J. Faes, I. Frerichs, H. Gagnon, Y. Gärber *et al.*, "Greit: a unified approach to 2d linear eit reconstruction of lung images," *Physiological measurement*, vol. 30, no. 6, p. S35, 2009.

[18] D. C. Barber and B. H. Brown, "Applied potential tomography," *Journal of Physics E: Scientific Instruments*, vol. 17, no. 9, pp. 723–733, sep 1984.

[19] S. Siltanen, J. Mueller, and D. Isaacson, "An implementation of the reconstruction algorithm of a nachman for the 2d inverse conductivity problem," *Inverse Problems*, vol. 16, no. 3, p. 681, 2000.

[20] J. Mueller, S. Siltanen, and D. Isaacson, "Special issue on electrical impedance tomography-reconstruction algorithms/data extraction-a direct reconstruction algorithm for electrical impedance tomography," *IEEE Transactions on Medical Imaging*, vol. 21, no. 6, pp. 555–559, 2002.

[21] J. L. Mueller and S. Siltanen, *Linear and nonlinear inverse problems with practical applications*. Siam, 2012, vol. 10.

[22] M. Alsaker, S. J. Hamilton, and A. Hauptmann, "A direct d-bar method for partial boundary data electrical impedance tomography with a priori information," *Inverse Problems & Imaging*, vol. 11, no. 3, pp. 427–454, 2017.

[23] X. Chen, *Computational Methods for Electromagnetic Inverse Scattering*. John Wiley & Sons, 2018.

[24] A. Nissinen, V. P. Kolehmainen, and J. P. Kaipio, "Compensation of modelling errors due to unknown domain boundary in electrical impedance tomography," *IEEE Transactions on Medical Imaging*, vol. 30, no. 2, pp. 231–242, 2011.

[25] J. Kaipio and E. Somersalo, *Statistical and computational inverse problems*. Springer Science & Business Media, 2006, vol. 160.

[26] S. J. Hamilton and A. Hauptmann, "Deep d-bar: Real time electrical impedance tomography imaging with deep neural networks," *IEEE Transactions on Medical Imaging*, vol. 37, no. 10, pp. 2367–2377, 2018.

[27] Z. Wei, D. Liu, and X. Chen, "Dominant-current deep learning scheme for electrical impedance tomography," *IEEE Transactions on Biomedical Engineering*, vol. 66, no. 9, pp. 2546–2555, 2019.

[28] A. K. Khambampati, K. Y. Kim, Y.-G. Lee, and S. Kim, "Boundary element method to estimate the time-varying interfacial boundary in horizontal immiscible liquids flow using electrical resistance tomography," *Applied Mathematical Modelling*, vol. 40, no. 2, pp. 1052–1068, 2016.

[29] A. Rashid, S. Kim, D. Liu, and K. Kim, "A dynamic oppositional biogeography-based optimization approach for time-varying electrical impedance tomography," *Physiological measurement*, vol. 37, no. 6, p. 820, 2016.

[30] B. Harrach, "Recent progress on the factorization method for electrical impedance tomography," *Comput Math Methods Med*, vol. 2013, no. 4, p. 425184, 2013.

[31] H. Ammari, *An introduction to mathematics of emerging biomedical imaging*. Springer, 2008, vol. 62.

[32] S. Ren, Y. Wang, G. Liang, and F. Dong, "A robust inclusion boundary reconstructor for electrical impedance tomography with geometric constraints," *IEEE Transactions on Instrumentation and Measurement*, vol. 68, no. 3, pp. 762–773, 2018.

[33] B. Harrach and M. N. Minh, "Enhancing residual-based techniques with shape reconstruction features in electrical impedance tomography," *Inverse Problems*, vol. 32, no. 12, p. 125002, 2016.

[34] ——, "Monotonicity-based regularization for phantom experiment data in electrical impedance tomography," in *New Trends in Parameter Identification for Mathematical Models*. Springer, 2018, pp. 107–120.

[35] M. Ikehata, "Enclosing a polygonal cavity in a two-dimensional bounded domain from cauchy data," *Inverse Problems*, vol. 15, no. 5, p. 1231, 1999.

[36] M. Ikehata and S. Siltanen, "Numerical method for finding the convex hull of an inclusion in conductivity from boundary measurements," *Inverse Problems*, vol. 16, no. 4, p. 1043, 2000.

[37] D. Liu and J. Du, "A moving morphable components based shape reconstruction framework for electrical impedance tomography," *IEEE transactions on medical imaging*, vol. 38, no. 12, pp. 2937–2948, 2019.

[38] S. Osher and J. A. Sethian, "Fronts propagating with curvature-dependent speed: algorithms based on hamilton-jacobi formulations," *Journal of computational physics*, vol. 79, no. 1, pp. 12–49, 1988.

[39] E. T. Chung, T. F. Chan, and X.-C. Tai, "Electrical impedance tomography using level set representation and total variational regularization," *Journal of Computational Physics*, vol. 205, no. 1, pp. 357 – 372, 2005.

[40] M. Soleimani, O. Dorn, and W. R. Lionheart, "A narrow-band level set method applied to eit in brain for cryosurgery monitoring," *IEEE transactions on biomedical engineering*, vol. 53, no. 11, pp. 2257–2264, 2006.

[41] D. Liu, A. K. Khambampati, S. Kim, and K. Y. Kim, "Multi-phase flow monitoring with electrical impedance tomography using level set based method," *Nuclear Engineering and Design*, vol. 289, pp. 108 – 116, 2015.

[42] V. Kolehmainen, M. J. Ehrhardt, and S. R. Arridge, "Incorporating structural prior information and sparsity into eit using parallel level sets," *Inverse Problems & Imaging*, vol. 13, no. 2, pp. 285–307, 2019.

[43] M. Soleimani, W. Lionheart, and O. Dorn, "Level set reconstruction of conductivity and permittivity from boundary electrical measurements using experimental data," *Inverse problems in science and engineering*, vol. 14, no. 2, pp. 193–210, 2006.

[44] E. Al Hosani and M. Soleimani, "Multiphase permittivity imaging using absolute value electrical capacitance tomography data and a level set algorithm," *Philosophical Transactions of the Royal Society A: Mathematical, Physical and Engineering Sciences*, vol. 374, no. 2070, p. 20150332, 2016.

[45] X. Niu, R. Vardavas, R. Caflisch, and C. Ratsch, "Level set simulation of directed self-assembly during epitaxial growth," *Physical Review B*, vol. 74, no. 19, p. 193403, 2006.

[46] A. Guittet, C. Poignard, and F. Gibou, "A voronoi interface approach to cell aggregate electropermeabilization," *Journal of Computational Physics*, vol. 332, pp. 143–159, 2017.

[47] O. Dorn and D. Lesselier, "Level set methods for inverse scattering," *Inverse Problems*, vol. 22, no. 4, pp. R67–R131, jun 2006.

[48] D. Liu, A. K. Khambampati, and J. Du, "A parametric level set method for electrical impedance tomography," *IEEE Transactions on Medical Imaging*, vol. 37, no. 2, pp. 451–460, 2018.

[49] D. Liu, Y. Zhao, A. Khambampati, A. Seppänen, and J. Du, "A parametric level set method for imaging multiphase conductivity using electrical impedance tomography," vol. 4, pp. 552–561, 12 2018.

[50] D. Liu, D. Smyl, and J. Du, "A parametric level set based approach to difference imaging in electrical impedance tomography," *IEEE Transactions on Medical Imaging*, vol. 38, no. 1, pp. 145–155, 2019.

[51] D. Liu, D. Gu, D. Smyl, J. Deng, and J. Du, "B-spline based sharp feature preserving shape reconstruction approach for electrical impedance tomography," *IEEE Transactions on Medical Imaging*, vol. 38, no. 11, pp. 2533–2544, 2019.

[52] O. Bernard, D. Friboulet, P. Thevenaz, and M. Unser, "Variational b-spline level-set: A linear filtering approach for fast deformable model evolution," *IEEE Transactions on Image Processing*, vol. 18, no. 6, pp. 1179–1191, 2009.

[53] V.-T. Pham, T.-T. Tran, K.-K. Shyu, L.-Y. Lin, Y.-H. Wang, and M.-T. Lo, "Multiphase b-spline level set and incremental shape priors with applications to segmentation and tracking of left ventricle in cardiac mr images," *Machine Vision and Applications*, vol. 25, no. 8, pp. 1967–1987, 2014.

[54] C. V. Verhoosel, G. Van Zwieten, B. Van Rietbergen, and R. de Borst, "Image-based goal-oriented adaptive isogeometric analysis with application to the micro-mechanical modeling of trabecular bone," *Computer Methods in Applied Mechanics and Engineering*, vol. 284, pp. 138–164, 2015.

[55] H. N. Nguyen, T. Y. Kam, and P. Y. Cheng, "Automatic crack detection from 2d images using a crack measure-based b-spline level set model," *Multidimensional Systems and Signal Processing*, vol. 29, no. 1, pp. 1–32, 2016.

[56] S. Cai, W. Zhang, J. Zhu, and T. Gao, "Stress constrained shape and topology optimization with fixed mesh: A b-spline finite cell method combined with level set function," *Computer Methods in Applied Mechanics and Engineering*, vol. 278, pp. 361 – 387, 2014.

[57] M. Y. Wang, H. Zong, Q. Ma, Y. Tian, and M. Zhou, "Cellular level set in b-splines (clibs): A method for modeling and topology optimization of cellular structures," *Computer Methods in Applied Mechanics and Engineering*, vol. 349, pp. 378–404, 2019.

[58] M. Eck and H. Hoppe, "Automatic reconstruction of b-spline surfaces of arbitrary topological type," in *Proceedings of the 23rd Annual Conference on Computer Graphics and Interactive Techniques*, ser. SIGGRAPH '96. New York, NY, USA: ACM, 1996, pp. 325–334.

[59] B. A. Barsky and D. P. Greenberg, "Determining a set of b-spline control vertices to generate an interpolating surface," *Computer Graphics and Image Processing*, vol. 14, no. 3, pp. 203 – 226, 1980.

[60] E. Somersalo, M. Cheney, and D. Isaacson, "Existence and uniqueness for electrode models for electric current computed tomography," *SIAM Journal on Applied Mathematics*, vol. 52, no. 4, pp. 1023–1040, 1992.

[61] P. Vauhkonen, M. Vauhkonen, T. Savolainen, and J. Kaipio, "Three-dimensional electrical impedance tomography based on the complete electrode model," *IEEE Trans. Biomed. Eng*, vol. 46, pp. 1150–1160, 1999.

[62] L. M. Heikkinen, T. Vilhunen, R. M. West, and M. Vauhkonen, "Simultaneous reconstruction of electrode contact impedances and internal electrical properties: Ii. laboratory experiments," *Measurement Science and Technology*, vol. 13, no. 12, p. 1855, 2002.

[63] F. Massarwi and G. Elber, "A b-spline based framework for volumetric object modeling," *Computer-Aided Design*, vol. 78, pp. 36–47, 2016.

[64] D. Liu, D. Smyl, and J. Du, "Nonstationary shape estimation in electrical impedance tomography using a parametric level set-based extended kalman filter approach," *IEEE Transactions on Instrumentation and Measurement*, To be published, 2019, dOI: 10.1109/TIM.2019.2921441.

[65] J. Kourunen, T. Savolainen, A. Lehikoinen, M. Vauhkonen, and L. Heikkinen, "Suitability of a pxi platform for an electrical impedance tomography system," *Measurement Science and Technology*, vol. 20, no. 1, p. 015503, 2009.

[66] Z. Wang, A. C. Bovik, H. R. Sheikh, and E. P. Simoncelli, "Image quality assessment: from error visibility to structural similarity," *IEEE transactions on image processing*, vol. 13, no. 4, pp. 600–612, 2004.

[67] D. Salomon, *Curves and surfaces for computer graphics*. Springer Science & Business Media, 2007.

[68] C. Harmening and H. Neuner, "Choosing the optimal number of b-spline control points (part 1: Methodology and approximation of curves)," *Journal of Applied Geodesy*, vol. 10, no. 3, pp. 139–157, 2016.

[69] ——, "Choosing the optimal number of b-spline control points (part 2: Approximation of surfaces and applications)," *Journal of Applied Geodesy*, vol. 11, no. 1, pp. 43–52, 2017.

[70] B. Harrach and J. K. Seo, "Exact shape-reconstruction by one-step linearization in electrical impedance tomography," *SIAM Journal on Mathematical Analysis*, vol. 42, no. 4, pp. 1505–1518, 2010.

[71] G. S. Alberti, H. Ammari, B. Jin, J.-K. Seo, and W. Zhang, "The linearized inverse problem in multifrequency electrical impedance tomography," *SIAM Journal on Imaging Sciences*, vol. 9, no. 4, pp. 1525–1551, 2016.

[72] H. Ammari, P. Garapon, F. Jouve, H. Kang, M. Lim, and S. Yu, "A new optimal control approach for the reconstruction of extended inclusions," *SIAM Journal on Control and Optimization*, vol. 51, no. 2, pp. 1372–1394, 2013.